An Integrated Modular Motor Drive with Shared Cooling for Axial Flux Motor Drives

Abdalla Hussein Mohamed, Hendrik Vansompel and Peter Sergeant, *Senior Member, IEEE*

***Abstract*—In this paper, a circumscribing polygon integrated modular motor drive topology with shared cooling for the power converter and the electrical machine is proposed, and benchmarked with the non-integrated version. The proposed topology is applied on an axial flux permanent magnet synchronous machine. The topology is capable of mechanically mounting the power converter, sufficiently cooling both the power converter and the electrical machine and combining both of them into the same housing. The mechanical and the thermal design are done to ensure thermal decoupling between the power converter and the motor winding and to provide a low thermal resistance from the power converter and the electrical machine to the ambient. Due to the limited space available for the power converter module, wide bandgap semiconductor technology is chosen for the implementation of the converter module thanks to their small package size and low power losses. A highly modular, integrated and compact drive is achieved compared to the non-integrated one. A CFD model is developed for one module of the proposed integrated drive to evaluate the maximum current that can be injected by one converter module without exceeding the junction temperature limit of the switches and the maximum winding temperature. An experimental setup is built to validate the results of the introduced multiphysics models.**

***Index Terms*—Integrated motor drives, Wide Bandgap devices, Thermal modelling, Power density, Axial flux machines.**

I. Introduction

THE integrated modular motor drives (IMMD) combine the benefits of both worlds of integrated and modular drives. The integrated drive is a physical integration of the motor and the driving power electronics into one unit [1].

This physical integration means a close proximity between the power electronics and the machine windings. This proximity leads to the elimination of the expensive and usually shielded cables needed to connect the power electronics to the motor in the conventional drives.

This structural integration involves a shared housing and cooling system for both the machine and the power electronics. The combined benefits of the elimination of the cables and the separate cooling and enclosure for the power electronics are reduced electromagnetic interference (EMI), reduced winding voltage stress caused by the surge impedance missmatch between the cables and the windings, volume and weight of the whole drive [2]- [3]. In terms of numbers, the elimination of such components can reduce the whole volume of the drive by 10%-20% [3]- [4].

In modular drives, the power electronics converter is divided into modules, each module is supplying a part of the stator windings. The modularity enhances the fault tolerance of the whole drive as each module can be controlled to contribute by certain amount to the whole torque by proper control. Moreover, the system can tolerate the fault in one or more module depending on the number of modules [5]. Having several converter modules sharing the power of the whole drive improves the thermal performance of the power electronics devices as the surface area used by the converter modules increases and requires a smaller voltage rated devices as well [6].

The IMMD adds many challenges on the design of the power converter module from the space and the thermal management point of view [7]- [8].

IMMD-topologies can be classified according to the position of the power converter into radially housing mounted (RHM), axially housing mounted (AHM), radially stator iron mounted (RSM) and axially stator iron mounted (ASM) [4].

In the RHM configuration, the power converter is mounted on the outer periphery of the machine in the radial direction in a separate enclosure. In [9], a RHM integrated motor drive is proposed for switched reluctance machines. The power converter is implemented as one unit in a separate housing sharing the same water cooling loop with the motor.

The RHM is more suitable for sausage design type of electrical machines where, the stack length is longer than the stator diameter. Despite of being a simple way for integration, the converter still needs its own separate housing which increases the diameter of the machine considerably.

In the AHM configuration, the power converter is mounted axially in a separate enclosure. In [10], a water cooled 6-phase inverter is designed for axial integration with a 6-phase machine. This configuration is suitable for pancake design type of electrical machines and it has the same merits and drawbacks of the RHM configuration.

The RSM and ASM configurations are providing more compact integrated drive topology while adding more challenges in the thermal management of the power converter due to the

Manuscript received Month xx, 2xxx; revised Month xx, xxxx; accepted Month x, xxxx. This work is part of the Flanders Make project SBO ModulAr. Abdalla H. Mohamed, H. Vansompel and P. Sergeant are with the Department of Electromechanical, Systems and Metal Engineering, Ghent University, 9000 Ghent, Belgium, and Flanders Make @UGent - core lab EEDT-MP, Belgium (e-mail: Abdalla.Mohamed@UGent.be). Abdalla H. Mohamed is also with Electrical power department (EPE), Faculty of Engineering, Cairo University, Cairo (e-mail:a.Hussien.Rashad@gmail.com)

close proximity to the major heat sources in the drive (the windings and the core).

In [2], a RSM 3-phase integrated drive is proposed for hybrid vehicles. The power converter is synthesized from 3-half bridge modules mounted on a water jacket separating between the power converter and the stator of the machine.

In [11], an ASM 5-phase integrated modular drive is proposed for switched reluctance machines where the power converter modules are mounted axially on a ring shaped heat sink sharing the same enclosure with the machine.

The design of the IMMD converter using WBG commercially available devices like the silicon carbide (SiC) or the Gallium nitride (GaN) can be of great benefit in having a high power density converter suitable for the IMMD challenges [12].

The smaller package size, lower losses, higher thermal conductivity and higher junction temperature of the WBG devices compared to the Si devices result in a much higher power density converter suitable for the IMMD stringent ambient conditions [13].

In this paper, a fully modularized integrated motor drive topology is proposed and designed for a double rotor single stator yokeless and segmented armature (YASA) axial flux permanent magnet synchronous machine (PMSM).

YASA axial flux machines are gaining popularity in many applications like electric vehicles and wind energy generation systems thanks to their high efficiency and power density [14].

The integration approach proposed in this paper provides a solution for the most challenging aspect of the integrated drives which is the thermal management of the power converter residing in close proximity to the electrical machine winding with its high heat generation. The topology proposed keeps the power converter modules close to the machine winding and efficiently decouple the heat generated by both of them.

One more advantage of the proposed topology is that it makes it possible to synthesize the full integrated drive from several identical pole drive units combining the machine stator parts, their associated driving converter and a shared cooling for both of them. In that way, the manufacturing process can be greatly simplified and a fully modular drive approach can be achieved.

The proposed topology is optimized from the thermal point of view in order to maximize the current that can be injected by the inverter modules. The maximum current that can be injected without exceeding the rated temperature of the switches and the winding insulation is calculated.

The paper is organized as follows: section II demonstrates the mechanical design of the proposed integration topology, section III explains the design of the WBG based discrete converter module, section IV calculates the maximum power of the proposed integration approach and the experimental results are given in section V.

II. Mechanical design of The proposed Integrated Drive

Fig. 1 shows the construction of the original non-integrated YASA machine. It consists of a number of coils of the concentrated winding type, where each coil consists of a copper winding wound around a silicon steel core. All the coils are arranged circumferentially, impregnated with epoxy resin and casted to form the active part of the stator with an aluminum housing around the stator to evacuate the heat generated by the stator elements to the ambient [15].

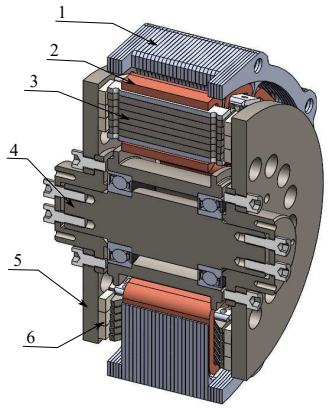

Fig. 1. Cross-section view of the non-integrated YASA prototype: (1) Housing, (2) Winding, (3) Core, (4) Shaft, (5) Rotor Disk, (6) PMs

TABLE I
THE KEY SPECIFICATIONS OF THE NON-INTEGRATED MACHINE

Quantity	Symbol	Value
Rated power (kW)	P	4
Rated speed (rpm)	n	2500
Rated rms current (A)	I_r	9
# Pair poles	p_r	8
# Slots	n_s	15
Axial length (mm)	L_{ax}	60
Outer diameter (mm)	D_{out}	190

The YASA machine has two-rotor disks with surface mounted permanent magnets (PMs).

Table. I lists the key specifications of the non-integrated machine.

Fig. 2 shows the geometry of the housing lamination of the non-integrated drive. It consists of a circular shaped outer periphery with inward fins in contact with the stator windings for more effective heat transfer to the ambient [15].

In order to utilize the same housing for cooling both the stator modules and the power converter modules, two-main modifications should be done to the housing: the first one is to introduce a flat surface on the housing to mechanically mount the power converter modules (mechanical reason) and to have a good contact between the switch thermal pad and the housing (thermal reason). The second one is to thermally decouple the stator modules and the power converter modules to avoid over temperature of the power modules.

Fig. 3 shows the proposed housing lamination construction for integrating the power modules and the machine. The outer surface of the housing lamination has been modified from

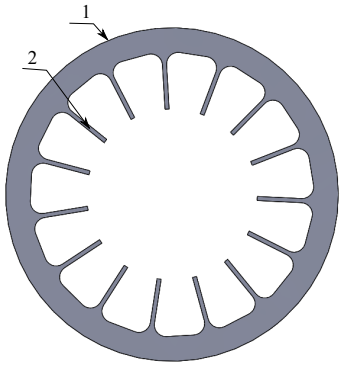

Fig. 2. The non-integrated drive housing lamination: (1) Outer circular periphery, (2) Stator heat extraction fins

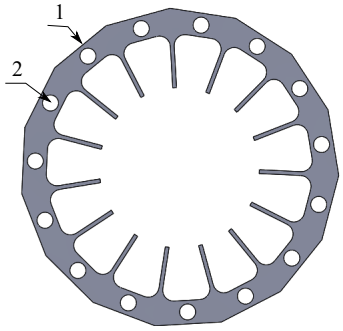

Fig. 3. The proposed housing lamination: (1) Flat surface for mounting the half-bridge modules, (2) Cooling channel

being circular to polygon shape. In that way, the converter modules can be mounted on the outer surface of the housing. Also, an axial cooling channel has been introduced between the stator module and the power converter module. By injecting a cooling fluid in the circular channels, the stator modules and the power converter modules will be thermally decoupled and the heat generated by both of them can be dissipated in the cooling fluid.

Since the axial length of the machine will be maintained, the dimension of the converter module PCB in the axial direction will be the same as the axial length of the machine (L_{ax}). The value of the other dimension (L_y) depends on the diameter of the inscribed circle which is the outer diameter (D_{out}) of the machine and the number of stator modules (n). The value of (L_y) can be calculated from (1).

$$L_y = D_{out} \tan(\frac{180}{n}) \tag{1}$$

The size of the resulted flat surface per module for the 15-phase case study is 40 mm in the circumferential direction and 60 mm in the axial direction. This means that the dimensions of the power converter module are limited to $(60 * 40)$ mm^2.

Fig. 4 shows the construction of the proposed integrated drive for the YASA machine. The stator module comprising the Converter PCB, the machine stator pole and the shared cooling can be manufactured as one unit and the whole stator can be synthesized from them.

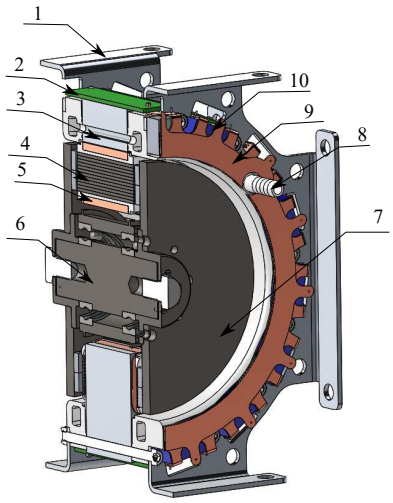

Fig. 4. The proposed integrated drive: (1) Mounting structure, (2) Converter module PCB, (3) Cooling channel, (4) Core, (5) Winding, (6) Shaft, (7) Rotor disk, (8) Cooling fluid injector, (9) DC link Bus bar, (10) DC link Capacitor

III. Design of The Power Converter Module

Due to the limited space available per converter module, the power electronics switches should be selected to have a small form factor and low power losses beside the electrical ratings suitable for the application.

A. Selection of the switching devices

GaN technology has been selected for the implementation of the integrated converter module due to their low figure of merit $(FOM = R_{ds} * Q_g)$ which is an indication for the low losses in the forward conduction path [16] and the zero reverse recovery charge which indicates a zero switching losses in the reverse conduction path.

B. Heat flux density of the power switches

For the choice of a GaN device for the converter implementation, the heat flux density of two commercial GaN devices *GS66508B* & *LMG341xR070* is evaluated at different modulation indices (M). The heat flux density is defined to be the total power losses generated by the switch during one fundamental power cycle divided by the case (thermal pad) area of the device. The heat flux density is considered for the calculation to consider the influence of the thermal pad area on the heat transfer from the switches.

The losses in the forward conduction path can be calculated from (2) [17].

$$\begin{cases} P_{tcond} & = I_{trms}^2 * R_{ds} \\ P_{ton} & = [V_{dc} f_o] * \\ & \sum_{n=1}^{m_f} (t_{on}(nT_s) i_{ton}(nT_s) + Q_{rr}(nT_s)) \\ P_{toff} & = [V_{dc} f_o] \sum_{n=1}^{m_f} t_{off}(nT_S) i_{toff}(nT_S) \\ P_{tf} & = P_{tcond} + P_{ton} + P_{toff} \end{cases} \tag{2}$$

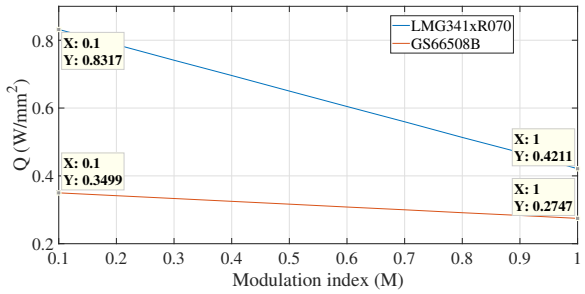

Fig. 5. The heat flux density for both GaN devices at unity PF versus the modulation index, SPWM.

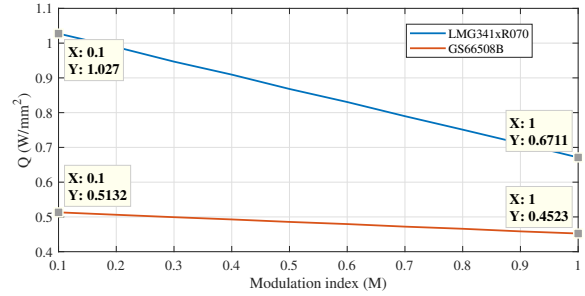

Fig. 6. The heat flux for both GaN devices at unity PF versus the modulation index, SVPWM.

where, P_{tcond} is the conduction losses in the forward conduction path, I_{trms} is the rms value of the transistor current, R_{ds} is the drain to source resistance of the switch, $f_o = \frac{p_r n_s}{60}$ is the fundamental output frequency, $m_f = \frac{f_s}{f_o}$ is the frequency modulation ratio, $t_{on}(nT_s)$ is the turn on transition time of the switch at the sample (n), $i_{ton}(nT_s)$ is the forward conduction current sampled at the rising edge of the gate signal, $t_{off}(nT_s)$ is the turn off transition time of the switch, $i_{toff}(nT_s)$ is the forward conduction current sampled at the falling edge of the gate signal. P_{tf} is the total losses in the forward conduction path.

The losses in the reverse conduction path can be calculated from (3).

$$P_d = f_o \int_t^{t+T_o} i_d(t) v_d(t) dt \tag{3}$$

where, $T_o = \frac{1}{f_o}$ is the fundamental power cycle, $i_d(t)$ is the instantaneous current in the reverse conduction path for one complete power cycle, $v_d(t)$ is the voltage drop in the reverse conduction direction for one power cycle, P_d is the loss in the reverse conduction path.

Due to the zero reverse recovery charge and reverse recovery current, the switching losses in the reverse conduction path are zero.

Figs. 5&6 show the heat flux density versus the modulation index for the two GaN switches at V_{dc} = 400V, I_{phase} = 9A, and switching frequency of 50kHz for sinusoidal pulse width modulation & space vector pulse width modulation respectively. Both curves are generated at 150°C junction temperature.

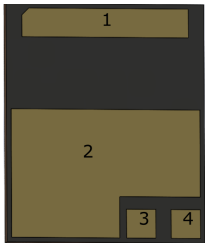

Fig. 7. *(GS66508B)* Package:(1) Drain, (2) Source, (3) Gate, (4) Source sense

By inspecting Figs. 5&6, the heat flux density of *(GS66508B)* is smaller than the other device and this makes it the best choice for the implementation of the integrated converter module. Also, the power losses generated at SPWM are lower than the SVPWM, which makes the SPWM a better choice for controlling the converter.

From the same figures, it can be observed that the power losses decrease with the modulation index. This can be explained by the significance of the losses in the reverse conduction path compared to the forward path due to the high voltage drop on the reverse path compared to the forward path. As the modulation index increases, the forward conduction duration prevails over the reverse one which means lower reverse losses and hence total losses reduction with the modulation index.

C. Thermal design of the converter module

The maximum power density that can be achieved by the proposed integrated drive topology depends on the maximum current that can be injected by the converter module without exceeding the maximum junction temperature of the switches.

The junction temperature of the switch depends not only on the junction power losses but also on the thermal impedance from the junction to the coolant. This thermal impedance has two components: one from the junction to the case and the other from the case to the coolant. The latter can be greatly reduced by a proper thermal design of the power converter board.

Fig. 7 shows the *(GS66508B)* package seen from the bottom.

Besides the electrical function of the source pin (pin 2), it also receives most of the heat generated in the switch die. So, the thermal impedance from the pin 2 (Fig. 7) to the coolant should be minimized.

The PCB is designed as a four-layer board for enhancing the electromagnetic and thermal performance of the whole converter [18].

Fig. 8 is a photo for the implemented half-bridge module.

The copper layers act as heat spreaders while the thermal vias reduce the thermal impedance of the heat path from the top layer to the bottom layer. Spreading the thermal vias beyond the thermal pad of the switch helps reducing the overall thermal impedance around the PCB [19].

Fig. 9 shows the copper plotted area beneath the thermal pad of the switch (See Fig. 7) with the thermal vias distributed around.

The copper area with the via pattern in Fig. 9 is included in the four copper layers.

Fig. 8. The implemented half-bridge module

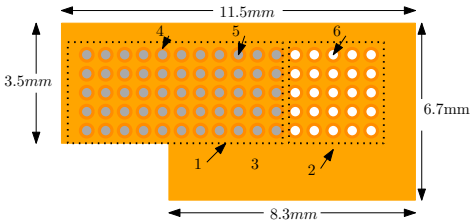

Fig. 9. The copper plotted area with the thermal vias pattern: (1) Zone1, the thermal vias underneath the switch thermal pad, (2) Zone2, the thermal vias pattern outside the thermal pad, (3) The copper area, (4) The via plating copper, (5) The via filling solder, (6) Air

TABLE II
THE THERMAL VIA DIMENSIONS

Quantity	Value
Via outer diameter (mm)	0.35
Thickness of via plating (μm)	25
Via spacing (mm)	0.65

TABLE III
THERMAL PROPERTIES OF PCB MATERIALS

Property	Copper (CU)	FR4	Air	Solder(SnAgCu)
Density (kg/m^3)	8890	1250	1.1614	7500
Specific heat capacity (J/kg.K)	392	1300	1005	250
Thermal conductivity(W/m.K)	385	0.35	0.0261	57.3

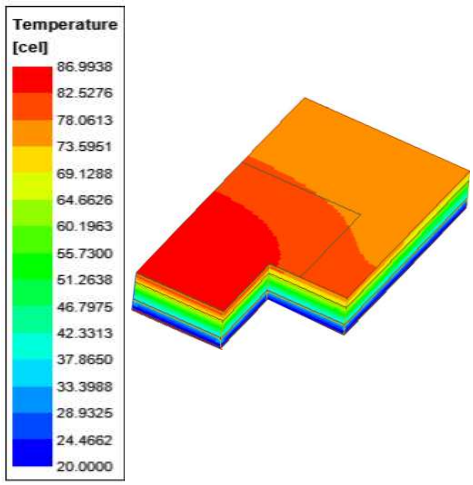

Fig. 10. The temperature distribution underneath the switch in case of no vias

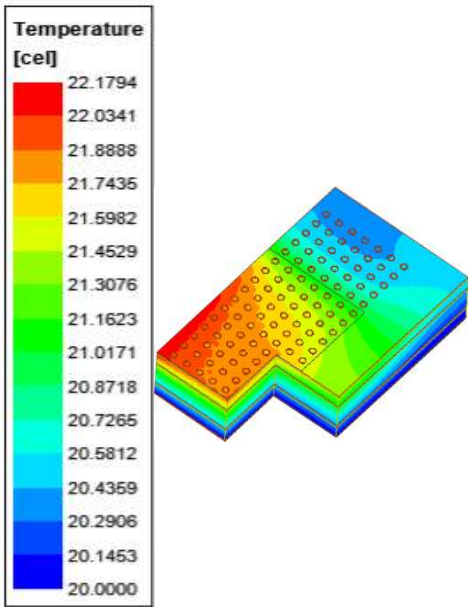

Fig. 11. The temperature distribution underneath the switch in case of vias

To evaluate the amount of thermal impedance reduction resulting from the via patterns in Fig. 9, two thermal finite element models have been built. One without the thermal vias and the other with them included. The dimensions of the copper plot area and the thermal via barrel are in Fig. 9 and table. II respectively. The material properties of the different parts are in table. III.

The boundary conditions are 1W of heat losses imposed on the top part of zone 1 (P_{sw}) (See Fig. 9) while the whole bottom surface is isothermal at temperature of ($T_{bottom} = 20°\text{C}$), the other surfaces are adiabatic.

Fig. 10 shows the temperature distribution of the model without thermal vias.

Equation (4) can be used to calculate the thermal resistance from the case of the switch to the bottom layer.

$$R_{th} = \frac{T_{case} - T_{bottom}}{P_{sw}} \tag{4}$$

where, T_{case} is the case temperature of the switch.

From Fig. 10, the maximum temperature of the switch case 86.9°C, this results in a thermal resistance of 66.9°C/W.

Fig. 11 shows the effect of the thermal vias on the maximum switch case temperature for the same boundary conditions. It can be seen that the maximum temperature reduced to 22.2°C which means a thermal resistance of 2.2°C/W and this amounts to a reduction of about 98.7% in the thermal resistance from the case of the switch to the bottom of the PCB.

This significant reduction in the thermal resistance will extremely increase the upper bound of the current that can be

supplied to the motor before reaching the junction temperature limit of the switch.

IV. Drive maximum Power per module

The maximum output power that can be achieved by the proposed drive is limited by the maximum junction temperature of the switches and the maximum temperature of the insulation of the windings.

The method used for the calculation of the power density of the proposed drive is as follows:

- Calculate the switch power losses that result in a junction temperature of 115°C, a margin of 35°C is left with zero winding and core losses.
- From the power losses versus temperature model of the power transistors, calculate the line current that results in the losses calculated in the previous step at 115°C.
- Calculate the machine losses (Winding and core) at the current calculated in step 2.
- Recalculate the switches junction temperature and the winding temperature with the machine power losses taken into account
- If the junction and the winding temperatures are within the limits, then consider the current calculated in step 2 as the maximum safe operating current,if not, reduce the current up to the level that keeps the temperature within the limit
- Calculate the maximum power per module from $V * I * PF$ where, V is the rms of the phase voltage, I is the rms of the current and PF is the power factor. The total drive power can be obtained by multiplying the result by the number of modules

To apply the above described method, a thermal model for one integrated drive module is needed along with a power loss model for the machine components and a power loss versus temperature model for the power switches.

The power loss of the machine components is calculated using the method of loss separation developed in [20].

A. Module CFD model

A CFD model is built for one drive module to calculate the switch losses at which the junction temperature of the switches is 115°C.

Fig. 12 shows the simulated geometry of one module.

The winding, the core and the housing of the machine have heterogeneous structures. Each consists of the main constituting material (i.e. copper in case of the windings, silicon steel for the core and aluminum for the housing), insulation around the wires and the laminations and epoxy for impregnation. The approach used for modelling such a heterogeneous structure is the Hashin-Shritkman approach for homogenization [21].

Equation (5) can be used to calculate the thermal conductivity of the winding, the core and the housing, where, $f_{(w,c)}$ is the winding or stacking factor, $K_{(w,c)}$ is the thermal conductivity of the main winding/core/housing material, K_e is the thermal conductivity of the impregnation material.

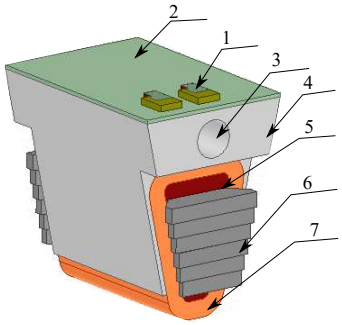

Fig. 12. The 3D module geometry: (1) the PCB, (2) the thermal interface material (TIM), (3) the cooling channel, (4) the housing, (5) the epoxy resin, (6) the core laminations, (7) the windings

TABLE IV
THE THERMAL PROPERTIES OF THE MATERIALS OF ONE MODULE

Module part	Material	ρ(kg/m^3)	C_p(J/kg.k)	K(W/m.K)
Winding	Copper	8890	392	385
Core	silicon steel	7650	490	40
Housing	Aluminum	2712	896	167
Impregnation	epoxy	1540	600	0.4
TIM	silicon compound	2750	710	4.4

Equations (6) & (7) can be used to calculate the specific heat capacity and mass density of the winding, the core and the housing, where, $C_{(w,c)}$ is the specific heat capacity of the winding/core/housing, C_e is the specific heat capacity of the impregnation, $\rho_{(w,c)}$ is the mass density of the winding/core/housing, ρ_e is the mass density of the impregnation epoxy.

$$\begin{cases} K_1 & = f_{w,c} * K_{w,c} + (1 - f_{w,c}) * K_e \\ & \rightarrow \text{lapping \& non-stacking directions} \\ K_2 & = K_e \frac{(1+f_{w,c})*K_{w,c}+f_{w,c}*K_e}{(1-f_{w,c})*K_{w,c}+(1+(1-f_{w,c}))*K_e} \\ & \rightarrow \text{other directions} \end{cases} \tag{5}$$

$$C_{ph} = f_{w,c} * C_{w,c} + (1 - f_{w,c}) * C_e \tag{6}$$

$$\rho_{ph} = f_{w,c} * \rho_{w,c} + (1 - f_{w,c}) * \rho_e \tag{7}$$

Table. IV contains the thermal properties of the different parts of one drive module.

The adiabatic boundary condition is used for all surfaces, the cooling fluid used is water with inlet temperature 22.5°C and flow rate of 1 L/min.

Fig. 13 shows the module temperature distribution resulted from 8.25W loss per switch and zero winding and core loss.

The maximum resulted case temperature at 8.25W losses per switch is 111.6°C, the thermal resistance of the switch from junction to case is 0.5°C/W which means a junction temperature of 115.7°C.

Fig. 14 shows the variation of the switch losses versus junction temperature at different line currents. From that figure, the maximum line current is 14A.

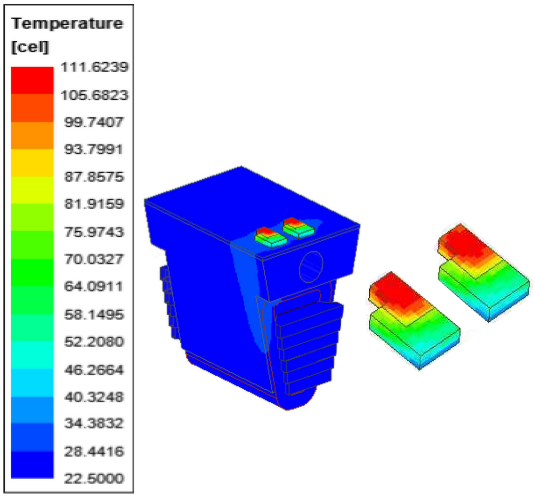

Fig. 13. The temperature distribution of one drive module at 8.25W switch losses and zero winding and core losses with switches temperature distribution zoomed

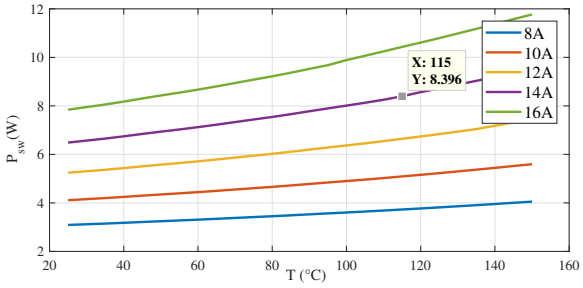

Fig. 14. The power losses per switch versus junction temperature at different peak line currents

The operating conditions considered for the generation of Fig. 14 are: SPWM, 400V DC link voltage, 2500 rpm speed, power factor of 0.85, switching frequency of 50kHz and unity modulation index.

The winding and the core losses are calculated at 14A peak line current considering coil resistance of 128mΩ at 100°C winding temperature. The electromagnetic models developed in [22] for the axial flux PMSM are used for the computation of the flux density distribution in the core and then the loss separation method developed in [20] is used for the core loss calculation. The resulted copper loss per module is 12.55W and the core loss per module is 3.7W. The simulation is done again considering the machine losses and the result is shown in Fig. 15.

From Fig. 15, the maximum switch case loss is 114.8°C and this results in 118.6°C maximum junction temperature which is still 31.4°C less than the junction rated temperature.

The maximum power per module is calculated, and rated at 1147.5W. This means that the 15-modules prototype machine can provide 17212W total power using the proposed integration topology.

The non-integrated drive was originally designed to have 4kW rated power at 2500rpm rated speed [23]. Besides the power enhancement, the elimination of the separate inverter

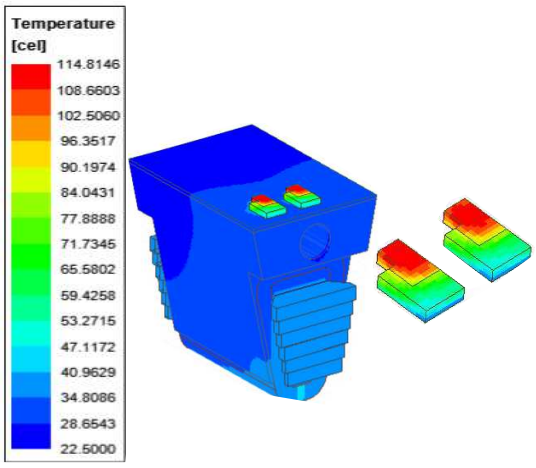

Fig. 15. The temperature distribution of one drive module at 8.25W switch losses with machine losses considered with the switches temperature distribution zoomed

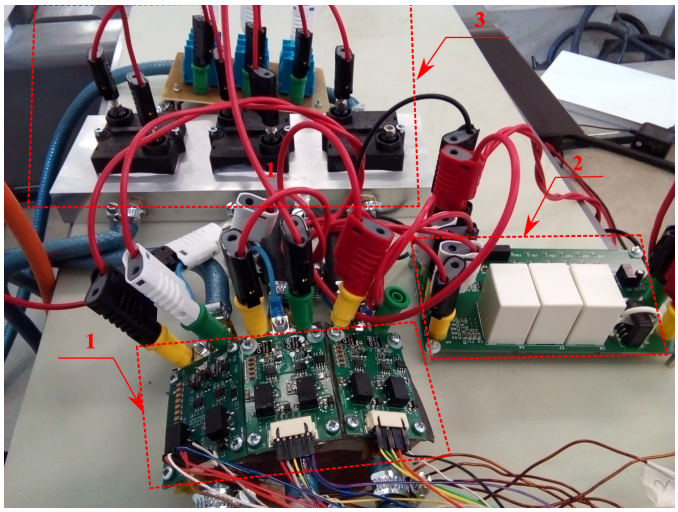

Fig. 16. Experimental setup: (1) The three teeth, (2) The DC link board, (3) The Load

cooling, its separate housing and the connection cables further reduces the overall weight and volume of the whole drive.

It can be noted from Fig. 15 that the maximum winding and core temperature are 41.5°C and 38.5°C respectively. This indicates that higher current can be injected in the windings before reaching the thermal limits of the windings insulation and this can be achieved by parallel connections of the GaN transistors to keep the junction temperature within the limit as well.

V. Experimental Results

A three teeth setup is built to validate the cooling efficiency of the proposed integration topology.

Fig. 16 shows a picture for the experimental setup.

The temperature of the switches is measured using a thermal camera and the temperature of the winding is recorded by a PT100 RTD sensor.

The experimental work is done using DC current to generate a well defined heat in the switches and the windings to validate

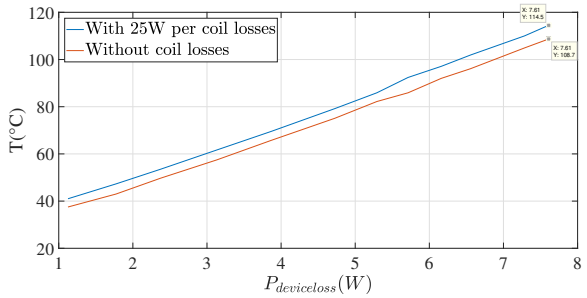

Fig. 17. The switch junction temperature versus losses at 1 L/min, 22.5°C inlet water temperature with and without coil losses

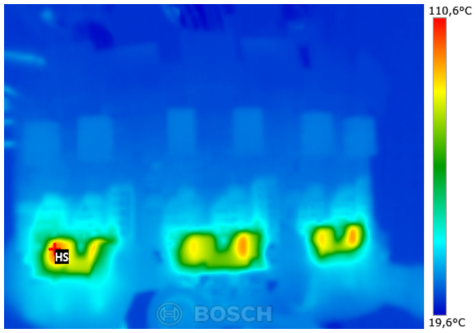

Fig. 19. The converter module temperature distribution at 7.6W loss per switch and 25W per coil losses at 1 L/min

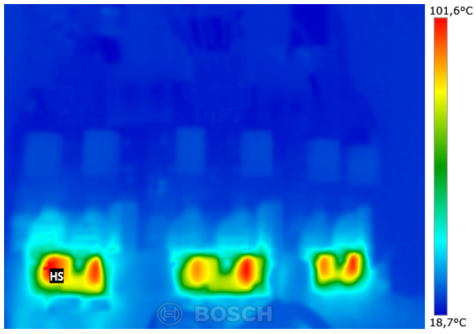

Fig. 18. The converter module temperature distribution at 7.6W loss per switch and zero winding losses at 1 L/min

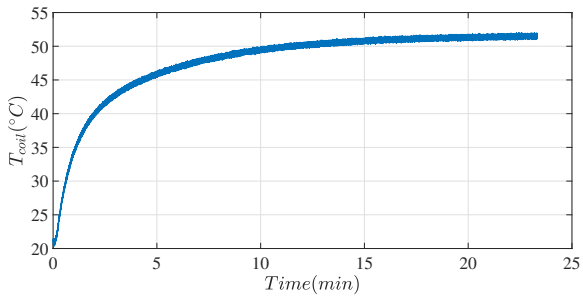

Fig. 20. The winding temperature versus time at 25W per coil losses and 7.6W per switch losses and 1 L/min

the CFD results and PWM waveforms to evaluate the validity of the DC thermal measurements at real waveforms. The DC measurements are performed as follows, the inverter switches and the winding of the three coils are heated by connecting the switches in series and supplying them from a DC source and the coils in series and supplying them from a separate DC source.

Fig. 17 shows the switch temperature versus power losses in case of zero and 25W losses per coil at 1 L/min and 22.5°C inlet water temperature. It can be seen from that figure that the junction temperature reaches 114.5°C at 7.6W switch losses and 25W per coil losses which proves the possibility to operate the switch up to that loss level safely. Note that the extrapolation of Fig. 17 results in a junction temperature of 116.55°C at 8.25W per switch loss compared to 115.7°C junction temperature estimated by CFD simulations in Fig. 13, a good agreement between the simulations and the measurements.

Figs. 18 & 19 show the temperature distribution on the power converter module without winding losses and with 25W per coil losses respectively at 1 L/min and 22.5°C water inlet temperature. In both cases, the loss per switch is 7.6W.

Note from Figs. 18 & 19 that the low power components on the converter PCB remain at low temperature which ensures high reliability of the converter module.

Fig. 20 shows the winding temperature at 25W per coil losses and 7.6W per switch losses, 1 L/min and 22.5°C water inlet temperature.

From Fig. 20, The steady state winding temperature at 25W coil losses is 52.8°C which proves an efficient winding cooling as well.

For evaluation of the validity of the thermal measurements performed with DC current and reported in Fig. 17, Fig. 18 and Fig. 19, the three inverter modules are operated as three phase inverter supplying an R = 8 Ω, L = 3 mH. The PWM pulses of 10kHz frequency are generated using the MicroLabBox dSPACE. The PWM technique used is the sinusoidal PWM. The windings of the three stator coils are not supplied directly from the inverter because of the small impedance of the coils resulting in the rated switch temperature at a few DC-link volts instead, a 25W loss per coil are generated by injecting a DC current in the windings.

Fig. 21 (a) shows the three phase currents measured with the on board sensor ACHS-7123 and filtered with an anti-aliasing filter of 1.7 kHz cut-off frequency. The waveforms are visualized with a 1GHz Tektronix scope. The peak value of the phase current I_{ph} is 9.55A (the rated current of the resistive part of the load is 7.5A) resulted at DC-link voltage of 175V. Fig. 21 (b) shows the line voltage.

The inverter input power is measured by multiplying the DC source current, measured by the current probe TCPA300 from Tektronix and shown in Fig. 22 (a) by the DC source voltage resulting in the waveform in Fig. 22 (b) with an average value of 1115W. The output power is calculated as $3I_{ph}^2R$ and the result is 1094.4W. The total loss of the three modules is 20.57W and the loss per switch is 3.42W. The measured switch temperature at these operating conditions is 63.2°C which from Fig. 17 (the curve with the winding losses considered) corresponds to a switch loss of 3.3W, an indication of the validity of the thermal performance measured with DC-

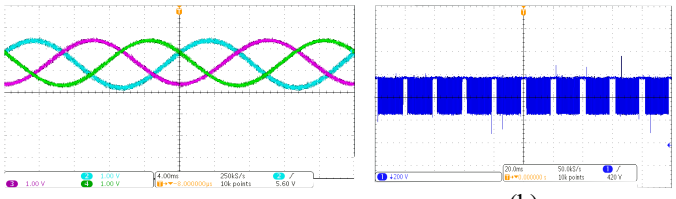

(a) (b)

Fig. 21. The PWM waveforms of the three module inverter (a) the three phase currents with 9.5A peak, (b) the line voltage with peak value of 175V

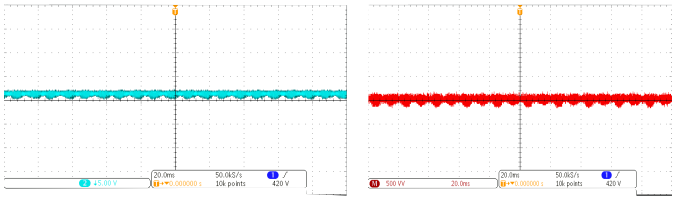

(a) (b)

Fig. 22. The DC source current/power waveforms of the three module inverter (a) the input current (b) the input power

current at the real PWM operating waveforms.

VI. Conclusion

A highly modular, integrated and compact motor drive is proposed in this paper and applied on a yokeless and segmented armature axial flux permanent magnet synchronous machine. The proposed integration topology is fully modular in the sense that the whole drive can be synthesized from the separate modules comprising the stator coil, the driving power converter module and the cooling system for both the machine and the converter module. The topology presents a feasible solution for the shared cooling of the inverter switches and the windings by efficiently decoupling and dissipating the heat of the switches and the windings by the same cooling circuit. The thermal design is optimized to get the maximum possible switch current without exceeding the junction and the winding insulation rated temperature. A discrete low form factor GaN based half-bridge module of 60×40 mm^2 size is designed and implemented. A CFD analysis has been performed for one drive module to calculate the maximum power per module. The module is capable of delivering up to 1147.5W at 400V DC link voltage. A much smaller drive with enhanced power compared to the conventional one is resulted. The experimental results are collected at DC and real PWM waveforms. The real PWM waveform thermal measurements confirm The DC measurements and both measurements confirm the CFD simulation results.

References

[1] M. Maerz, E. Schimanek, and M. Billmann, "Towards an Integrated Drive for Hybrid Traction," no. September, pp. 3–7, 2008.

[2] M. Maerz, M. Poech, E. Schimanek, and A. Schletz, "Mechatronic Integration into the Hybrid PowertrainâThe Thermal Challenge," *Proc. 1th International Conference on Automotive Power Electronics (APE)*, no. June, pp. 2–7, 2006. [Online]. Available: http://www.ecpe.org/download/publications/Paper{_}Maerz{_}APE2006.pdf

[3] R. Abebe, G. Vakil, G. L. Calzo, T. Cox, S. Lambert, M. Johnson, C. Gerada, and B. Mecrow, "Integrated motor drives: State of the art and future trends," *IET Electric Power Applications*, vol. 10, DOI 10.1049/iet-epa.2015.0506, no. 8, pp. 757–771, 2016.

[4] W. Lee, S. Li, D. Han, B. Sarlioglu, T. A. Minav, and M. Pietola, "A Review of Integrated Motor Drive and Wide-Bandgap Power Electronics for High-Performance Electro-Hydrostatic Actuators," *IEEE Transactions on Transportation Electrification*, vol. 4, DOI 10.1109/TTE.2018.2853994, no. 3, pp. 684–693, 2018.

[5] B. Ioana, R. Mircea, and S. Loránd, "Modular Electrical Machines â A Survey," no. 15, pp. 6–11, 2015.

[6] J. Wang, Y. Li, and Y. Han, "Evaluation and design for an integrated modular motor drive (IMMD) with GaN devices," *2013 IEEE Energy Conversion Congress and Exposition, ECCE 2013*, DOI 10.1109/ECCE.2013.6647278, no. Immd, pp. 4318–4325, 2013.

[7] N. R. Brown, T. M. Jahns, and R. D. Lorenz, "Power converter design for an integrated modular motor drive," *Conference Record - IAS Annual Meeting (IEEE Industry Applications Society)*, DOI 10.1109/IAS.2007.205, pp. 1322–1328, 2007.

[8] L. De Lillo, B. Ahmadi, L. Empringham, M. Johnson, J. Espina, and R. Abebe, "Next Generation Integrated Drive, NGID: A Novel Approach to Thermal and Electrical Integration of High Power Density Drives in Automotive Applications," *2018 IEEE Energy Conversion Congress and Exposition, ECCE 2018*, DOI 10.1109/ECCE.2018.8558001, pp. 1228–1232, 2018.

[9] A. Tenconi, F. Profumo, S. E. Bauer, and M. D. Hennen, "Temperatures evaluation in an integrated motor drive for traction applications," *IEEE Transactions on Industrial Electronics*, vol. 55, DOI 10.1109/TIE.2008.2003099, no. 10, pp. 3619–3626, 2008.

[10] G. Engelmann, M. Kowal, and R. W. De Doncker, "A highly integrated drive inverter using DirectFETs and ceramic dc-link capacitors for open-end winding machines in electric vehicles," *Conference Proceedings - IEEE Applied Power Electronics Conference and Exposition - APEC*, vol. 2015-May, DOI 10.1109/APEC.2015.7104365, no. May, pp. 290–296, 2015.

[11] M. D. Hennen, M. Niessen, C. Heyers, H. J. Brauer, and R. W. De Doncker, "Development and control of an integrated and distributed inverter for a fault tolerant five-phase switched reluctance traction drive," *IEEE Transactions on Power Electronics*, vol. 27, DOI 10.1109/TPEL.2011.2132763, no. 2, pp. 547–554, 2012.

[12] S. Hazra, S. Madhusoodhanan, S. Bhattacharya, G. K. Moghaddam, and K. Hatua, "Design considerations and performance evaluation of 1200 V, 100 a SiC MOSFET based converter for high power density application," *2013 IEEE Energy Conversion Congress and Exposition, ECCE 2013*, DOI 10.1109/ECCE.2013.6647272, pp. 4278–4285, 2013.

[13] A. H. Wijenayake, K. J. Olejniczak, D. Simco, S. Minden, M. Feurtado, B. Passmore, T. McNutt, A. Lostetter, and D. Martin, "Design of a 250 kW, 1200 v SiC MOSFET-Based three-Phase inverter by considering a subsystem level design optimization approach," *2017 IEEE Energy Conversion Congress and Exposition, ECCE 2017*, vol. 2017-Janua, DOI 10.1109/ECCE.2017.8095886, pp. 939–946, 2017.

[14] C. Du-Bar, "Design of an axial flux machine for an in-wheel motor application," *Chalmers Reproservice, Göteborg*, pp. 1–2, 2011. [Online]. Available: http://webfiles.portal.chalmers.se/et/MSc/DubarChristian.pdf

[15] H. Vansompel, P. Leijnen, and P. Sergeant, "Multiphysics Analysis of a Stator Construction Method in Yokeless and Segmented Armature Axial Flux PM Machines," *IEEE Transactions on Energy Conversion*, vol. 34, DOI 10.1109/TEC.2018.2862622, no. 1, pp. 139–146, 2019.

[16] D. Reusch, D. Gilham, Y. Su, and F. C. Lee, "Gallium Nitride based 3D integrated non-isolated point of load module," *Conference Proceedings - IEEE Applied Power Electronics Conference and Exposition - APEC*, DOI 10.1109/APEC.2012.6165796, pp. 38–45, 2012.

[17] M. Amyotte, E. S. Glitz, C. G. Perez, and M. Ordonez, "GaN Power Switches: A Comprehensive Approach to Power Loss Estimation," *2018 IEEE Energy Conversion Congress and Exposition, ECCE 2018*, DOI 10.1109/ECCE.2018.8557635, pp. 1926–1931, 2018.

[18] D. Reusch and J. Strydom, "Understanding the effect of PCB layout on circuit performance in a high frequency gallium nitride based point of load converter," *Conference Proceedings - IEEE Applied Power Electronics Conference and Exposition - APEC*, DOI 10.1109/APEC.2013.6520279, pp. 649–655, 2013.

[19] Y. Shen, H. Wang, F. Blaabjerg, H. Zhao, and T. Long, "Thermal modeling and design optimization of PCB vias and pads," *IEEE Transactions on Power Electronics*, vol. 35, DOI 10.1109/TPEL.2019.2915029, no. 1, pp. 882–900, 2020.

[20] G. Bertotti, "General Properties of Power Losses in Soft Ferromagnetic Materials." *IEEE Transactions on Magnetics*, vol. 24, DOI 10.1109/20.43994, no. 1, pp. 621–630, 1987.

[21] P. Romanazzi, M. Bruna, and D. A. Howey, "Thermal homogenization of electrical machine windings applying the multiple-scales method," *Journal of Heat Transfer*, vol. 139, DOI 10.1115/1.4034337, no. 1, pp. 1–8, 2017.

[22] A. Hemeida and P. Sergeant, "Analytical modeling of surface PMSM using a combined solution of Maxwell-s equations and magnetic equivalent circuit," *IEEE Transactions on Magnetics*, vol. 50, DOI 10.1109/TMAG.2014.2330801, no. 12, 2014.

[23] H. Vansompel, A. Yarantseva, P. Sergeant, and G. Crevecoeur, "An inverse thermal modeling approach for thermal parameter and loss identification in an axial flux permanent magnet machine," *IEEE Transactions on Industrial Electronics*, vol. 66, DOI 10.1109/TIE.2018.2838089, no. 3, pp. 1727–1735, 2019.

Abdalla H. Mohamed received the MSc degree in electrical power and machines engineering from Cairo University, Cairo, Egypt, in 2016. Currently, he is working as a PhD researcher at Ghent University, Belgium. His research interests are design of integrated modular motor drives, Power converters , and multi-physics modelling of electrical machines.

Hendrik Vansompel was born in Belgium in 1986. He received the MSc and PhD degrees in electromechanical engineering from Ghent University, Ghent, Belgium, in 2009 and 2013, respectively. He is currently a Postdoctoral Research Assistant with the Department of Electromechanical, Systems and Metal Engineering, Ghent University. His research interests include electric machines and power electronics.

Peter Sergeant received the MSc degree in electromechanical engineering in 2001, and the PhD degree in electromechanical engineering in 2006, both from Ghent University, Ghent, Belgium. In 2006, he became a postdoctoral researcher at Ghent University (postdoctoral fellow of the Research Foundation - Flanders). Since 2012, he is associate professor at Ghent University. He is also core lab manager in the cluster Motion Products of Flanders Make. His research domain is electrical machines and drives for industrial and for sustainable energy applications. The focus is on accurate computation of losses in machines